crystals

MDPI

Communication

Influence of Precursor Density and Conversion Time on the Orientation of Vapor-Deposited ZIF-8

Marianne Kräuter [1,*], Alexander John Cruz [2], Timothée Stassin [2], Sabina Rodríguez-Hermida [2], Rob Ameloot [2], Roland Resel [1] and Anna Maria Coclite [1]

[1] Institute of Solid State Physics, NAWI Graz, Graz University of Technology, Petersgasse 16, 8010 Graz, Austria; roland.resel@tugraz.at (R.R.); anna.coclite@tugraz.at (A.M.C.)
[2] Center for Membrane Separations, Adsorption, Catalysis, and Spectroscopy (cMACS), KU Leuven, Celestijnenlaan 200F, 3001 Leuven, Belgium; alex.cruz@kuleuven.be (A.J.C.); timothee.stassin@kuleuven.be (T.S.); sabina.rodriguez@udc.es (S.R.-H.); rob.ameloot@kuleuven.be (R.A.)
* Correspondence: marianne.kraeuter@tugraz.at; Tel.: +43-316-873-8467

Abstract: ZIF-8 was synthesized by subjecting ZnO thin films deposited via plasma-enhanced atomic layer deposition to a 2-methylimidazole vapor. The impact of the conversion time as well as the density and thickness of the ZnO precursor on the resulting ZIF-8 layers were investigated. Grazing Incidence X-ray diffraction reveals a preferred (100) or (111) orientation of the ZIF-8 crystals, depending on thickness and density of the precursor, and with a more prominent orientation at longer conversion times. The onset of crystallization occurs after 20 min of conversion for the less dense precursor, compared to 40 min for the denser one. The ZIF-8 thickness and roughness increase with conversion time. The final thickness of the ZIF-8 layer depends on the thickness and density of the precursor layer, and can be up to 15-fold higher than the precursor thickness.

Keywords: vapor phase conversion; zeolitic imidazole framework; PE-ALD; zinc oxide; metal-organic framework

Citation: Kräuter, M.; Cruz, A.J.; Stassin, T.; Rodríguez-Hermida, S.; Ameloot, R.; Resel, R.; Coclite, A.M. Influence of Precursor Density and Conversion Time on the Orientation of Vapor-Deposited ZIF-8. *Crystals* **2022**, *12*, 217. https://doi.org/10.3390/cryst12020217

Academic Editors: Jesús Sanmartín-Matalobos and Eamor M. Woo

Received: 2 December 2021
Accepted: 28 January 2022
Published: 1 February 2022

1. Introduction

Metal-organic frameworks (MOFs) are nanoporous crystalline materials that consist of metal nodes connected via organic linker molecules [1]. Due to the combination of long-range order, highly tunable organic-inorganic structural units, and intrinsic nanoporosity [2], the use of MOFs has been investigated in numerous fields, including but not limited to catalysis [3,4], storage and release of gases [5–7], molecular separation [8,9], drug delivery [10–12], and membranes for desalination [13]. Furthermore, MOFs show potential in microelectronics [14], as low-k dielectrics [15], sensor coatings [16–18], for energy conversion [19], or photonic crystals [20].

However, due to the complexity of the traditional solvothermal synthesis methods, MOFs are not often used in these fields due to risks related to chemical contamination, corrosion, and cost [21]. To incorporate MOFs into microelectronic devices, scalable thin-film deposition processes such as chemical vapor deposition (CVD) or atomic layer deposition (ALD) are essential [22,23]. These techniques are based on the reaction of vaporized substances on a substrate to form a thin film with a precisely controlled thickness. In particular, ALD allows for sub-nm thickness control in thin-film properties [24].

Up to now, to the best of our knowledge, vapor-phase-deposited ZIF-8 has only been synthesized in polycrystalline forms without exhibiting a preferred orientation, or crystalline texture [25,26]. Oriented ZIF-8 has been previously synthesized via solution-based methods, mainly with a preferential {100} [27,28], (110) [29] or (112) [30,31] orientation.

Here, we adapted the MOF-CVD method first demonstrated by Stassen et al. [32], in which a metal oxide layer is first grown via ALD and subsequently subjected to the vapor of the desired organic linker, resulting in MOF thin films. The process has shown

good reproducibility and compatibility with lithographic processes. Plasma-enhanced ALD (PE-ALD) offers the additional advantage of tuning the substrate temperature over a broad range, from room temperature to over 200 °C, by utilizing a reactive plasma species as the co-reactant. This parameter influences the crystal orientation of the ZnO thin films, leading to a preferred (100)-orientation of the ZnO precursor by keeping the substrate at room temperature (RT) [33].

For this work, we investigated the influence of the conversion time of PE-ALD deposited ZnO thin films to ZIF-8 and show how different precursor densities and thicknesses affect the final films. An overview of the varied deposition parameters and of the studied ZIF-8 properties is noted in Table S1.

2. Materials and Methods

2.1. Synthesis of ZIF-8

ZnO films were deposited in a custom direct plasma ALD reactor onto one-side polished c-Si (100) substrates (Siegert Wafer, Aachen, Germany) for 6 cycles, 17 cycles, and 60 cycles to obtain different thicknesses. The reactor was in an asymmetrical plate configuration with the heating stage (Yuheng Electric Heating Technology Co., Ltd., Yancheng, China) 5 cm below the showerhead radiofrequency (RF) electrode at 13.56 MHz. For a schematic of the reactor configuration, see Figure S1. The pumping system consisted of a turbomolecular pump (Pfeiffer vacuum, Aßlar, Germany, TmH071P) and a rotary vane pump (Pfeiffer vacuum, Aßlar, Germany, DUO5M). Diethylzinc (DEZ, Sigma-Aldrich, St. Louis, MI, USA, CAS 557-200) was pulsed into the reactor using an ALD valve (Swagelok, Solon, OH, USA, ALD3) without additional heating or bubbling system. During the plasma step, pure oxygen (Air liquide, Paris, France, 99.9995%) was used, supplied by an RF-power generator (Advanced Energy, Denver, CO, USA, Cesar 13.56 MHz) combined with a matching network (Advanced Energy, Denver, CO, USA Navio). Argon (Air liquide, Paris, France, 99.9995%) was employed in the purging step. The flow rates for O_2 and Ar were 20 sccm during the plasma and purging steps, and the O_2 pressure in the reactor during plasma exposure was fixed at 85 mTorr. To control the flow rates of the gases, a multi-gas controller (MKS Instruments, Andover, MA, USA, 647C) and mass flow controllers (MKS Instruments, Andover, MA, USA MF1-C) were used.

The PE-ALD process consisted of the following four steps, repeated for each cycle: (1) DEZ dose, (2) Ar purging, (3) O_2-plasma dose (including a 10 s O_2-flow stabilization step before the plasma ignition), and (4) Ar purging. To activate the substrate surface, the process was started with an O_2-plasma dose. The RF-power for the plasma dose was fixed at 60 W for all depositions. The substrate temperature during the depositions was kept at room temperature.

To deposit less dense ZnO, the heating stage was removed from the reactor, resulting in an increased interelectrodal distance of 7 cm. To follow the saturation behavior of the four steps as previously investigated [24,33], the recipe was fixed for deposition at room temperature at 0.15 s for the DEZ dose, 15 s for both Ar purges, and 8 s for the O_2-plasma dose. The setup was controlled by an Arduino microcontroller and an in-house written Python program [34].

To obtain ZIF-8, the ZnO thin films were placed into a 300 mL Schlenk tube together with a glass boat containing 500 mg of 2-methylimidazole (HmIm) powder (Merck, Darmstadt, Germany, 99%). The tube was closed and evacuated (to ~10^{-1} mbar). The Schlenk tube was placed in a convection preheated oven for different time periods (20 min to 24 h) at 120 °C. Afterward, the samples were removed from the tube while still hot and left to cool under a fume hood.

2.2. Characterization Methods

The density of ZnO was measured by X-ray reflectivity (XRR) with a Panalytical Empyrean (Malvern Panalytical, Malvern, United Kingdom) working in θ/θ-configuration and equipped with a copper tube (λ = 1.5418 Å). The primary side of the reflectometer was

equipped with a 1/32° slit, a 10 mm beam mask, a multilayer mirror, and an automatic beam attenuator. On the secondary side, a receiving slit of 0.1 mm and a Soller slit of 0.02 rad were placed before the point detector, Panalytical Pixel 3D. XRR scans were performed in the 2θ region 0.024°–5.00° with a step size of 0.008°. The XRR scans were characterized by a plateau of total reflection up to the critical angle of the material. The model used to evaluate the XRR data consisted of three materials (Si-SiO_2-ZnO), which all contribute with their critical angle. The critical angle of the substrate (0.22°), measured at the half of the plateau's maximum, is typical for the silicon dioxide interface [35].

Attenuated total reflection Fourier-transform infrared spectroscopy (ATR-FTIR) spectra were recorded on a Varian 670 FTIR spectrometer equipped with a Ge crystal plate in the VeeMAX III module (Pike Technologies, Fitchbur, WI, USA); 64 scans were accumulated by a DLaTGS detector with a resolution of 4 cm^{-1}.

Grazing incidence X-ray diffraction (GIXD) measurements were conducted at the beamline XRD1, Elettra, Trieste, Italy. The incident angle was set between 0.2° and 1.2°; the wavelength of the primary beam was 1.4 Å. Diffracted intensities were collected on a Pilatus 2M detector, and all data have been recalculated to (wavelength-independent) reciprocal space maps utilizing the in-house developed software package GIDVis [36]. Intensities are plotted in a pseudo-color representation as a function of the out-of-plane component (q_z) and the in-plane component (q_{xy}) of the scattering vector. For the sake of clarity and comparability, all intensity data were plotted in square root representation and are reported using the same color scales.

Scanning Electron Microscopy (SEM) images were collected using Philips (Amsterdam, Netherlands) XL30 FEG at an acceleration voltage of 10 kV and a working distance of 10 mm. The data was evaluated using the open source program ImageJ [37].

The optical properties of the ZIF-8 thin films were measured using an M-2000x spectroscopic ellipsometer (J.A. Woollam Co., Inc., Lincoln, NE, USA λ = 246–1000 nm) at a fixed 65° incidence angle. Each sample was remeasured four times on a different spot with an M-2000V ellipsometer (J.A. Woollam Co., Inc., Lincoln, NE, USA λ = 370–1000 nm) at three different incident angles (65°, 70°, and 75°) for error estimation. All ZnO layers were measured on the M-2000V ellipsometer in the same manner. The raw ellipsometry data were fitted using the CompleteEASE software (J. A. Woollam Co., Inc., Lincoln, NE, USA) in the whole measurement range employing a Cauchy model.

Additional thickness measurements were performed for ZIF-8 with an AlphaStep D-500 Profilometer (KLA-Tencor, Munich, Germany). Profilometry scanning parameters were set to a scan length of 0.5 mm, a speed of 0.05 mm/s, and a stylus force of 1 mg. The height values were obtained by scratching the sample to the substrate and measuring the step height from the substrate to the top of the layer. Measurements were performed at three different spots on each sample to estimate a statistical error.

Atomic Force Microscopy (AFM) measurements were conducted in non-contact mode with a PPP-NCLR-10 cantilever (NanoWorld AG, Neuchâtel, Switzerland) on a Nanosurf easyScan 2 instrument for the samples obtained from denser ZnO. ZIF-8 obtained from less dense ZnO was measured in the intermittent contact mode with a PicoSPM 5500 (Agilent Technologies, Santa Clara, CA, USA) setup in ambient conditions using Si cantilevers (OLYMPUS, Shinjuku, Japan, AC160TS-R3). Data analysis was performed using the freely available software package Gwyddion [38].

3. Results and Discussion

During the PE-ALD depositions, two different interelectrode distances were employed to obtain ZnO with different mass densities. Via spectroscopic ellipsometry the thicknesses of the resulting ZnO thin films were determined to (0.8 ± 0.1) nm, (2.9 ± 0.2) nm and (9.8 ± 0.5) nm for the less dense ZnO deposited for 6, 17, and 60 cycles, respectively. The denser ZnO showed thicknesses of (0.9 ± 0.2) nm, (2.8 ± 0.2) nm, and (9 ± 1) nm for the same amount of deposition cycles. These values agree well with the growth rate of approx. 1.6 Å for depositions at room temperature as reported in literature [33].

To investigate the density of the ZnO thin films, X-ray reflectivity (XRR) measurements were performed. Figure 1 shows XRR data of two different ZnO layers deposited for 60 cycles and their respective fit, marked in red. From the fit, the parameters of the less dense ZnO were determined to a thickness of (9.2 ± 0.1) nm with a roughness of (1.1 ± 0.1) nm and a mass density of (4.6 ± 0.1) g/cm^3. For the denser precursor, a thickness of (8.1 ± 0.1) nm, a roughness of (1.1 ± 0.1) nm, and a density of (5.2 ± 0.2) g/cm^3 were found. Both densities are lower than the literature value of 5.6 g/cm^3 reported for bulk ZnO [39].

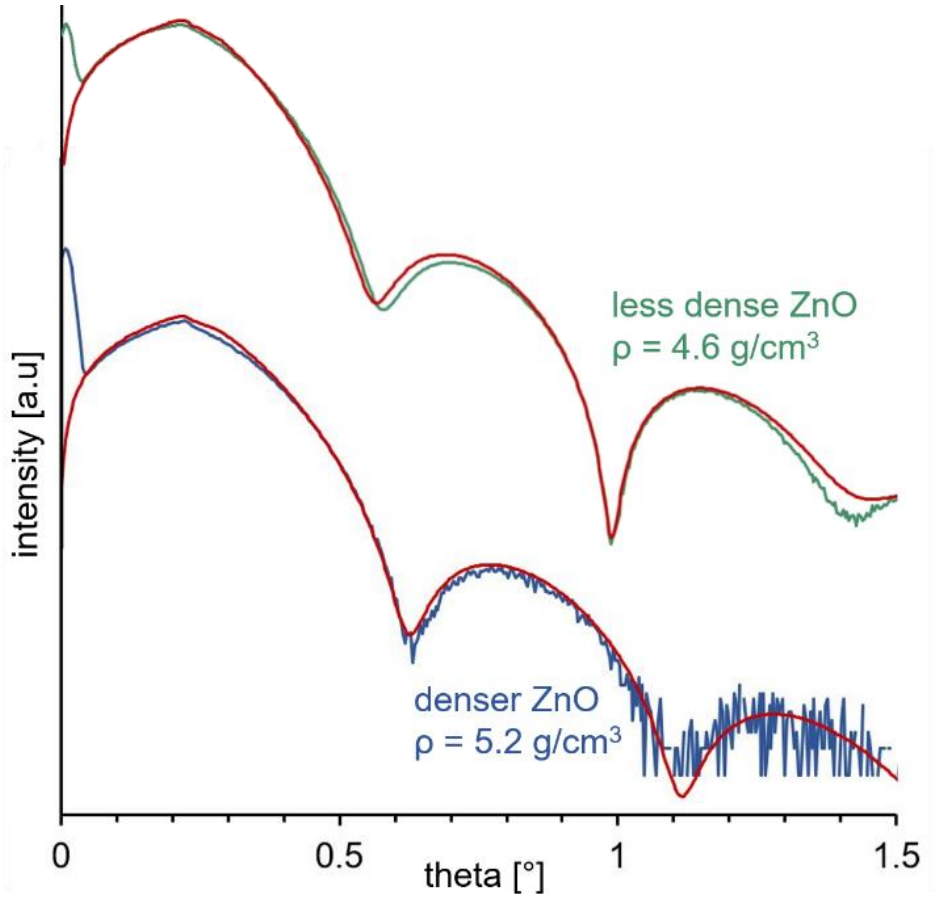

Figure 1. X-ray reflectivity measurements of ZnO thin films deposited for 60 cycles, showing different mass densities. Red lines correspond to fits.

After converting the ZnO layers to ZIF-8, ATR-FTIR measurements verify that the obtained layers match the chemical fingerprint of ZIF-8 (Figure S2). Successful synthesis of ZIF-8 was further confirmed with grazing incidence X-ray diffraction (GIXRD) measurements (Figure 2a). At short conversion times, no Bragg peaks are observed, as is the case for ZIF-8 grown from denser ZnO, deposited for 60 cycles, measured after 20 min of conversion. As the conversion time increases, Debye-Scherrer rings associated with a random orientation of ZIF-8 crystals appear (Figure S3a). With the conversion time increasing, intensity variations within the Debye-Scherrer rings are observed, indicating the development of a preferred orientation. The observation of a crystal ripening phase occurring after conversion of the sample coincides with previous findings [25].

Distinct Debye-Scherrer rings appear for the ZIF-8 from less dense ZnO deposited for 60 cycles already after 20 min of conversion (Figure 2a), in contrast to 40 min for the denser ZnO (Figure S3a). This observation indicates that the less dense precursor converts faster, and the onset of crystal ripening occurs earlier in that case, likely due to a higher hydroxyl defect density [40]. ZIF-8 samples obtained from less dense ZnO and thinner precursors (6 and 17 ZnO cycles) exhibit bright spots in addition to the Debye-Scherrer rings (Figure 2a),

thus indicating a preferred (100) orientation. Additionally, ZIF-8 obtained from denser ZnO and from thicker precursors exhibits intensity variations along the Debye-Scherrer rings, pointing towards a preferred (111) orientation. The measurements of ZIF-8 converted from ZnO deposited for 17 cycles in Figure 2a have been indexed accordingly to showcase the obtained preferred orientations. For permeation purposes, the (111) orientation is most favorable for ZIF-8, as this orientation causes its six-membered ring-windows to align parallel with the substrate (Figure S4b), whereas the (100) orientation leads to parallel alignment of the smaller four-membered ring windows (Figure S4a) [27].

The GIXRD measurements do not only differ in their preferred orientation but also regarding their mosaicity: ZIF-8 from denser and thicker ZnO results in broad arcs instead of distinct spots, showing that the crystallites are spread more widely around the dominant preferred crystal plane orientation than for ZIF-8 from thin, less dense ZnO. To estimate the mosaicity, the half-width at full maximum of intensity peaks within one Debye-Scherrer ring was measured, resulting in a low mosaicity of $(1.8 \pm 0.3)^\circ$ for the (100)-oriented ZIF-8 layers and a significantly larger mosaicity of $(29.6 \pm 1.4)^\circ$ for the (111)-oriented layers, showing a less pronounced preferred orientation of the latter samples.

Previous studies in which ZIF-8 was synthesized via the MOF-CVD method resulted in powder-like GIXRD patterns characteristic of random crystallite orientations [25]. Obtaining a preferred orientation shows that the nucleation, growth, and crystal ripening of ZIF-8 are influenced by the ZnO precursor and conversion time.

It has been shown that the presence of water augments the conversion and crystal ripening of ZIF-8 by enhancing the mobility of the MOF building blocks, which results in easier access of the linker to the precursor [32,41]. However, due to our conversion taking place in an evacuated vessel with the linker in form of a dry powder for all processed samples, we can rule out differences in the humidity level. It is speculated that the distinct (100) orientation is due to facilitated linker access for the ultra-thin ZnO layers–as opposed to thicker precursor layers–paired with a higher defect rate for the less dense ZnO, leading to enhanced crystallization. Furthermore, scanning electron microscopy (SEM) images (Figure 2b and Figure S5a) show that groups of ZIF-8 particles are obtained for the thinnest precursor layers instead of continuous thin films as is the case for the thicker ZnO films. This could indicate enhanced mobility for the ZIF-8 particles from very thin precursor layers, which might also lead to more pronounced crystallization.

A possible explanation for the observation of the broad (111) orientation for ZIF-8 from thicker and denser ZnO layers can be found in the "modified competitive growth model" as proposed by Bons and Bons [42]. In the classical competitive growth model, crystals–starting from randomly oriented nuclei–with the fastest growth direction perpendicular to the plane of the substrate will dominate in the film [43], which corresponds to <100> for ZIF-8 [27]. However, Bons and Bons argue that oblique orientations can occur when tilted crystals grow sideways in the early stages of crystallization, and thus cover their competitors [42]. The observed (111) orientation could be attributed to a kinetically hindered crystallization phase for these samples.

The effect of conversion time is also visible in SEM measurements (Figure 2b). Particles form on the substrate after 20 to 40 min and grow larger over conversion time. For ZIF-8 from the thickest precursor layers, the particles exhibit lateral diameters of (82 ± 24) nm from the denser and (184 ± 76) nm from the less dense ZnO, indicating that the precursor density also influences the final size of the observed ZIF-8 islands. This observation agrees with the atomic force microscopy (AFM) data in a recent report [40]. Since the conversion is faster for less dense ZnO, more distinct crystal ripening occurs. The surface coverage depends on the precursor thickness. For the thinnest ZnO layers, the resulting ZIF-8 layer consists of disconnected particles (Figure S5a). As the precursor thickness increases, the ZIF-8 particles grow in size and agglomerate, resulting in closed layers for the thickest investigated precursor layers.

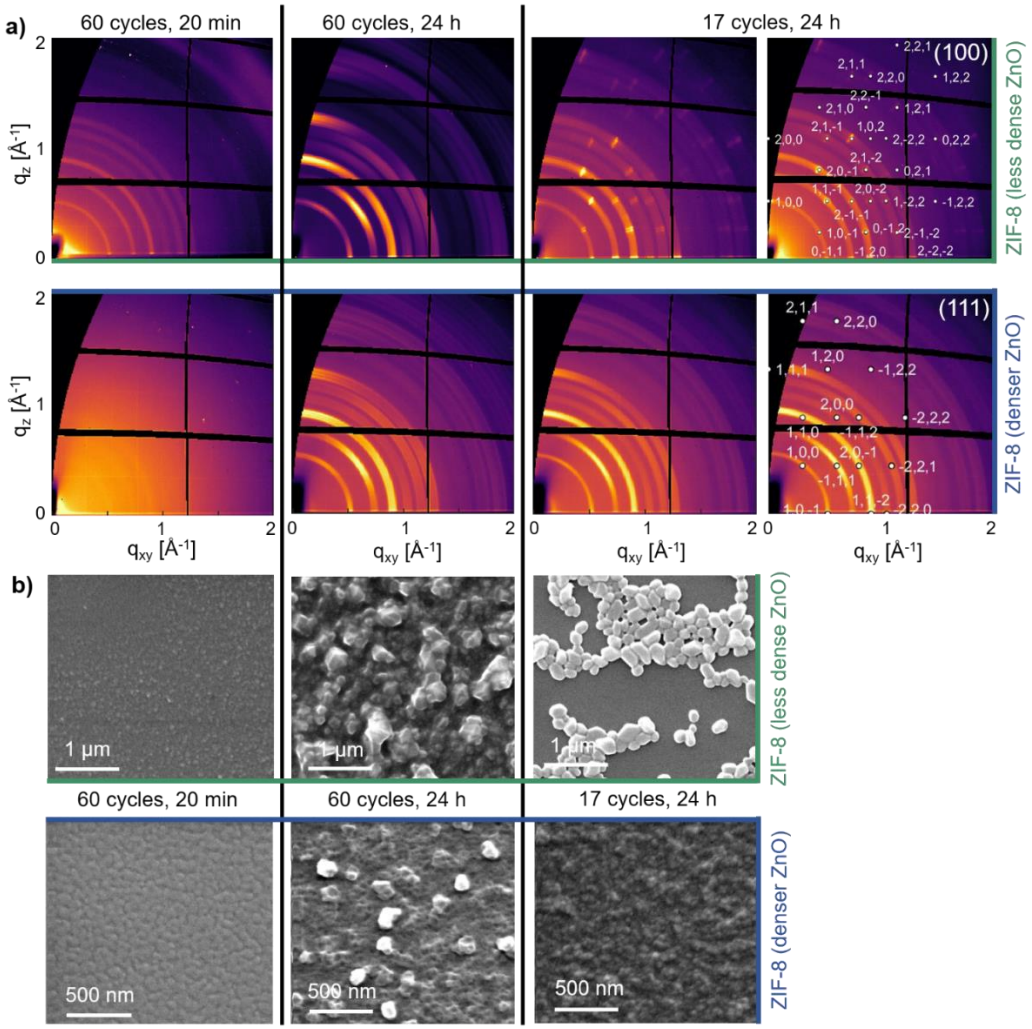

Figure 2. (**a**) ZIF-8 obtained after 20 min and 24 h of conversion from ZnO deposited for 60 and 17 cycles with densities of $\rho = (4.6 \pm 0.1)$ g/cm^3 and of $\rho = (5.2 \pm 0.2)$ g/cm^3 measured via grazing incidence X-ray diffraction. The diffraction patterns on the right are indexed with ZIF-8 reference data [44]; (**b**) Corresponding scanning electron microscopy images of the presented samples.

The development of the surface roughness was investigated via AFM; corresponding topography images can be found in Figure S6. Figure 3a shows RMS roughness values of ZIF-8 synthesized from denser ZnO: Up to 20 min of conversion time, the RMS roughness lies below 2 nm for all samples. After 40 min of conversion, the roughness increases in accordance with the conversion time as well as with precursor thickness. Even after 24 h of conversion, the roughness lies below 5 nm for ZIF-8 obtained from ZnO deposited for 6 and 17 cycles. Additional measurements conducted on ZIF-8 samples obtained from less dense ZnO indicate that less dense precursor results in significantly rougher layers. RMS values of (38 ± 6) nm and (41 ± 8) nm for ZIF-8 from less dense ZnO deposited for 17 cycles and deposited for 60 cycles, respectively, were measured in contrast to the significantly lower (5 ± 1) nm and (19 ± 6) nm for ZIF-8 from denser ZnO deposited for 17 cycles and 60 cycles, respectively. The mean particle height of ZIF-8 from denser ZnO deposited for 17 cycles was determined to (16 ± 1) nm and to (93 ± 6) nm for the less dense ZnO. The trend continues for ZIF-8 synthesized from ZnO deposited for 60 cycles, leading to a mean particle height of (53 ± 4) nm for the denser ZnO and (122 ± 3) nm for the less dense ZnO. These results are in accordance with the SEM images in Error! Reference source not found.b, which indicated that less dense ZnO leads to more extensive ripening, hence larger ZIF-8 particles.

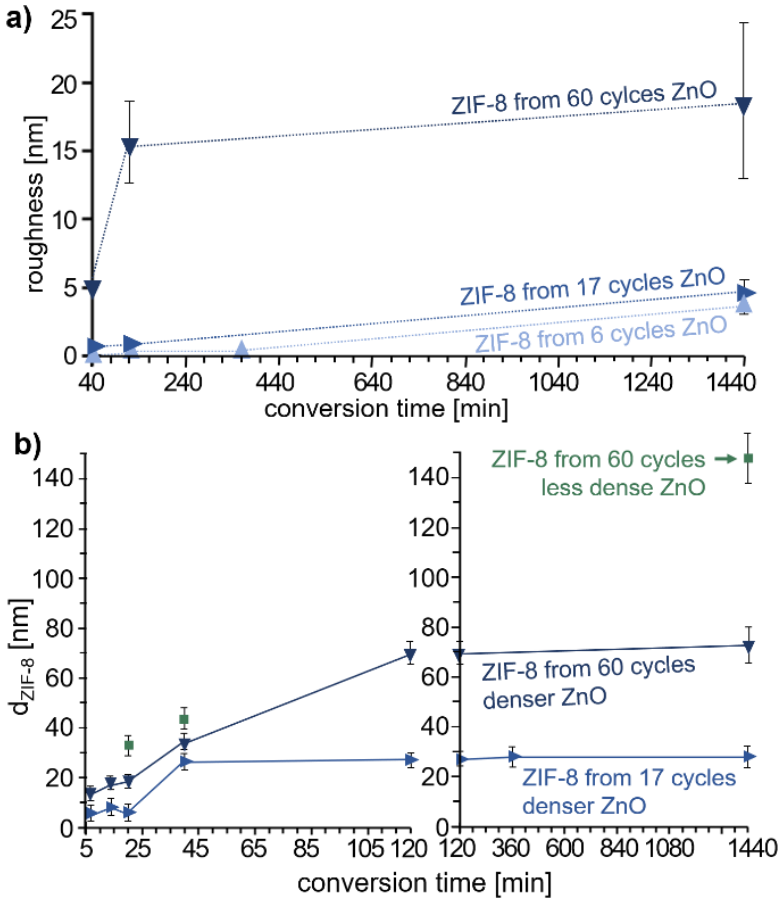

Figure 3. (**a**) RMS roughness of ZIF-8 obtained from ZnO with a density of $\rho = (5.2 \pm 0.2)$ g/cm^3, depending on the employed conversion time; (**b**) Thickness of ZIF-8 (d_{ZIF-8}) depending on conversion time measured via spectroscopic ellipsometry. Measured for ZIF-8 obtained from ZnO with densities of $\rho = (4.6 \pm 0.1)$ g/cm^3 and of $\rho = (5.2 \pm 0.2)$ g/cm^3.

Spectroscopic ellipsometry measurements performed for the continuous ZIF-8 layers show that the thickness of ZIF-8 (Figure 3b) increases in accordance with conversion time until a saturation point is reached, which depends on the thickness of the sacrificial ZnO layer. Whereas ZIF-8 from denser ZnO deposited for 17 cycles reaches its final thickness after 40 min, a thickness plateau is reached after 2 h for the thickest, denser precursor layers. This observation matches the impressions from the GIXRD that the conversion is completed after these times. The fact that the roughness still increases slightly (Figure 3a), even after the layer thickness has reached its plateau, points toward crystal ripening taking place.

Different thickness increases are reported for the conversion of ZIF-8 from ZnO thin films ranging from 10-fold [25] and about 17-fold [32], depending on the precursor, conversion time, linker vapor concentration, and reactor type. Here, a 15-fold thickness increase for ZIF-8 synthesized from less dense ZnO deposited for 60 cycles was observed. A lower thickness increase was detected for ZIF-8 obtained from denser ZnO, namely 8-fold (for the 60 cycle ZnO) and about 10-fold (for 17 cycle ZnO). The observation that denser layers result in less complete conversion has been made in previous studies and is attributed to the less deep penetration of the organic linker into the precursor layer during the conversion process. It seems that the precursor is less defective and therefore not as reactive [40]. The thickness of ZIF-8 rises with increasing ZnO thickness, reaching up to a final thickness of (148 ± 10) nm for less dense ZnO and (73 ± 7) nm for denser ZnO, both deposited for 60 cycles. These values correlate well with profilometry measurements resulting in (154 ± 5) nm for ZIF-8 from less dense ZnO and (73 ± 2) nm for ZIF-8 from denser ZnO.

4. Conclusions

In summary, ZIF-8 was synthesized via a solvent-free two-step vapor deposition process, based on PE-ALD followed by oxide-to-MOF conversion. GIXRD reveals a preferred (100) or (111) orientation of the formed ZIF-8 films, depending on the thickness and density of the ZnO precursor. Low-density ZnO leads to an earlier onset of crystallization and results in a higher roughness, crystallite size, and thickness increase during conversion. The coverage, thickness, roughness, and crystallite size of the ZIF-8 layers increase with the conversion time and with increasing ZnO thickness.

Supplementary Materials: The following are available online at https://www.mdpi.com/article/10.3390/cryst12020217/s1, Figure S1: Schematics of the reaction chamber of the plasma-enhanced atomic layer deposition set-up, Figure S2: Fourier-transform infrared spectroscopy data of ZIF-8, Figure S3: Additional GIXRD images, Figure S4: Schematics of different orientations of ZIF-8, plotted in Mercury [45], Figure S5: Additional SEM images, Figure S6: AFM topography images, Table S1. Overview of the varied deposition parameters and of the properties of the synthesized ZIF-8.

Author Contributions: Conceptualization, M.K., A.J.C., R.A., R.R. and A.M.C.; investigation, M.K., A.J.C. and T.S.; data curation, M.K., R.A., R.R. and A.M.C.; writing—original draft preparation, M.K.; writing—review and editing, M.K., A.J.C., T.S., S.R.-H., R.A., R.R. and A.M.C. All authors have read and agreed to the published version of the manuscript.

Funding: The financial support of the Lead project LP-03 "Porous Materials@Work" of the Graz University of Technology is gratefully acknowledged. T.S. thanks the Research Foundation Flanders (FWO) for an SB-PhD fellowship (1S53316N).

Data Availability Statement: Not applicable.

Acknowledgments: The authors thank the synchrotron ELETTRA, Trieste, Italy for the allocation of beamtime at the beamline XRD1, and especially the on-site beamtime scientist Luisa Barba as well as Benedikt Schrode. Additionally, the provision of a part of the ZnO samples by Alberto Perrotta and Julian Pilz is gratefully acknowledged. Open Access Funding by the Graz University of Technology. Open Access Funding by the Graz University of Technology.

Conflicts of Interest: The authors declare no conflict of interest.

References

1. Caro, J. Quo Vadis, MOF? *Chem. Ing. Tech.* **2018**, *90*, 1759–1768. [CrossRef]
2. Stassen, I.; De Vos, D.; Ameloot, R. Vapor-Phase Deposition and Modification of Metal–Organic Frameworks: State-of-the-Art and Future Directions. *Chem.-A Eur. J.* **2016**, *22*, 14452–14460. [CrossRef] [PubMed]
3. Lee, J.; Farha, O.K.; Roberts, J.; Scheidt, K.A.; Nguyen, S.T.; Hupp, J.T. Metal-organic framework materials as catalysts. *Chem. Soc. Rev.* **2009**, *38*, 1450–1459. [CrossRef] [PubMed]
4. Gascon, J.; Corma, A.; Kapteijn, F.; Llabrés I Xamena, F.X. Metal organic framework catalysis: Quo vadis? *ACS Catal.* **2014**, *4*, 361–378. [CrossRef]
5. Tian, T.; Velazquez-Garcia, J.; Bennett, T.D.; Fairen-Jimenez, D. Mechanically and chemically robust ZIF-8 monoliths with high volumetric adsorption capacity. *J. Mater. Chem. A* **2015**, *3*, 2999–3005. [CrossRef]
6. Abbasi, Z.; Shamsaei, E.; Fang, X.Y.; Ladewig, B.; Wang, H. Simple fabrication of zeolitic imidazolate framework ZIF-8/polymer composite beads by phase inversion method for efficient oil sorption. *J. Colloid Interface Sci.* **2017**, *493*, 150–161. [CrossRef] [PubMed]
7. Mason, J.A.; Veenstra, M.; Long, J.R. Evaluating metal-organic frameworks for natural gas storage. *Chem. Sci.* **2014**, *5*, 32–51. [CrossRef]
8. Kwon, H.T.; Jeong, H.K. In situ synthesis of thin zeolitic-imidazolate framework ZIF-8 membranes exhibiting exceptionally high propylene/propane separation. *J. Am. Chem. Soc.* **2013**, *135*, 10763–10768. [CrossRef]
9. Bae, Y.; Mulfort, K.L.; Frost, H.; Ryan, P.; Punnathanam, S.; Broadbelt, L.J.; Hupp, J.T.; Snurr, R.Q. Separation of CO_2 from CH_4 Using Mixed-Ligand Metal—Organic Frameworks. *Langmuir* **2008**, *24*, 8592–8598. [CrossRef]
10. Della Rocca, J.; Liu, D.; Lin, W. Nanoscale metal-organic frameworks for biomedical imaging and drug delivery. *Acc. Chem. Res.* **2011**, *44*, 957–968. [CrossRef]
11. Horcajada, P.; Chalati, T.; Serre, C.; Gillet, B.; Sebrie, C.; Baati, T.; Eubank, J.F.; Heurtaux, D.; Clayette, P.; Kreuz, C.; et al. Porous metal-organic-framework nanoscale carriers as a potential platform for drug deliveryand imaging. *Nat. Mater.* **2010**, *9*, 172–178. [CrossRef] [PubMed]

12. Orellana-Tavra, C.; Baxter, E.F.; Tian, T.; Bennett, T.D.; Slater, N.K.H.; Cheetham, A.K.; Fairen-Jimenez, D. Amorphous metal-organic frameworks for drug delivery. *Chem. Commun.* **2015**, *51*, 13878–13881. [CrossRef] [PubMed]
13. Duke, M.C.; Zhu, B.; Doherty, C.M.; Hill, M.R.; Hill, A.J.; Carreon, M.A. Structural effects on SAPO-34 and ZIF-8 materials exposed to seawater solutions, and their potential as desalination membranes. *Desalination* **2016**, *377*, 128–137. [CrossRef]
14. Stassen, I.; Campagnol, N.; Fransaer, J.; Vereecken, P.; De Vos, D.; Ameloot, R. Solvent-free synthesis of supported ZIF-8 films and patterns through transformation of deposited zinc oxide precursors. *CrystEngComm* **2013**, *15*, 9308–9311. [CrossRef]
15. Eslava, S.; Zhang, L.; Esconjauregui, S.; Yang, J.; Vanstreels, K.; Baklanov, M.R.; Saiz, E. Metal-organic framework ZIF-8 films as low-κ dielectrics in microelectronics. *Chem. Mater.* **2013**, *25*, 27–33. [CrossRef]
16. Zhao, H.; Li, X.; Li, W.; Wang, P.; Chen, S.; Quan, X. A ZIF-8-based platform for the rapid and highly sensitive detection of indoor formaldehyde. *RSC Adv.* **2014**, *4*, 36444–36450. [CrossRef]
17. Wang, D.; Li, Z.; Zhou, J.; Fang, H.; He, X.; Jena, P.; Zeng, J.-B.; Wang, W.-N. Simultaneous Detection and Removal of Formaldehyde at Room Temperature: Janus Au@ZnO@ZIF-8 Nanoparticles. *Nano-Micro Lett.* **2018**, *10*, 4. [CrossRef]
18. Lu, G.; Hupp, J.T. Metal-organic frameworks as sensors: A ZIF-8 based fabry-pérot device as a selective sensor for chemical vapors and gases. *J. Am. Chem. Soc.* **2010**, *132*, 7832–7833. [CrossRef]
19. Ryder, M.R.; Tan, J.C. Nanoporous metal organic framework materials for smart applications. *Energy Mater. Mater. Sci. Eng. Energy Syst.* **2014**, *9*, 1598–1612. [CrossRef]
20. Avci, C.; Imaz, I.; Carné-Sánchez, A.; Pariente, J.A.; Tasios, N.; Pérez-Carvajal, J.; Alonso, M.I.; Blanco, A.; Dijkstra, M.; López, C.; et al. Self-assembly of polyhedral metal-organic framework particles into three-dimensional ordered superstructures. *Nat. Chem.* **2018**, *10*, 78–84. [CrossRef]
21. Stassin, T.; Rodríguez-Hermida, S.; Schrode, B.; Cruz, A.J.; Carraro, F.; Kravchenko, D.; Creemers, V.; Stassen, I.; Hauffman, T.; De Vos, D.; et al. Vapour-phase deposition of oriented copper dicarboxylate metal–organic framework thin films. *Chem. Commun.* **2019**, *55*, 10056–10059. [CrossRef] [PubMed]
22. Allendorf, M.D.; Schwartzberg, A.; Stavila, V.; Talin, A.A. A roadmap to implementing metal-organic frameworks in electronic devices: Challenges and critical directions. *Chem.-A Eur. J.* **2011**, *17*, 11372–11388. [CrossRef] [PubMed]
23. Stassen, I.; Burtch, N.; Talin, A.; Falcaro, P.; Allendorf, M.; Ameloot, R. An updated roadmap for the integration of metal-organic frameworks with electronic devices and chemical sensors. *Chem. Soc. Rev.* **2017**, *46*, 3185–3241. [CrossRef] [PubMed]
24. Pilz, J.; Perrotta, A.; Christian, P.; Tazreiter, M.; Resel, R.; Leising, G.; Griesser, T.; Coclite, A.M. Tuning of material properties of ZnO thin films grown by plasma-enhanced atomic layer deposition at room temperature. *J. Vac. Sci. Technol. A Vac. Surf. Film.* **2018**, *36*, 01A109. [CrossRef]
25. Cruz, A.J.; Stassen, I.; Krishtab, M.; Marcoen, K.; Stassin, T.; Rodríguez-hermida, S.; Teyssandier, J.; Pletincx, S.; Verbeke, R.; Rubio-, V.; et al. An integrated cleanroom process for the vapor phase deposition of large-area zeolitic imidazolate framework thin films. *Chem. Mater.* **2019**, *31*, 9462–9471. [CrossRef]
26. Tanaka, S.; Sakamoto, K.; Inada, H.; Kawata, M.; Takasaki, G.; Imawaka, K. Vapor-Phase Synthesis of ZIF-8 MOF Thick Film by Conversion of ZnO Nanorod Array. *Langmuir* **2018**, *34*, 7028–7033. [CrossRef]
27. Bux, H.; Feldhoff, A.; Cravillon, J.; Wiebcke, M.; Li, Y.S.; Caro, J. Oriented zeolitic imidazolate framework-8 membrane with sharp H 2/C3H8 molecular sieve separation. *Chem. Mater.* **2011**, *23*, 2262–2269. [CrossRef]
28. Sharma, S.K.; Utpalla, P.; Bahadur, J.; Goutam, U.K.; Pujari, P.K. Micrometer scale pore-interconnectivity in nanoporous ZIF-8 films with Zn enriched surface terminations. *Microporous Mesoporous Mater.* **2020**, *307*, 110519. [CrossRef]
29. Shekhah, O.; Eddaoudi, M. The liquid phase epitaxy method for the construction of oriented ZIF-8 thin films with controlled growth on functionalized surfaces. *Chem. Commun.* **2013**, *49*, 10079–10081. [CrossRef]
30. Zhu, M.; Jasinski, J.B.; Carreon, M.A. Growth of zeolitic imidazolate framework-8 crystals from the solid-liquid interface. *J. Mater. Chem.* **2012**, *22*, 7684–7686. [CrossRef]
31. Liu, C.; Sun, F.; Zhou, S.; Tian, Y.; Zhu, G. Facile synthesis of ZIF-8 nanocrystals in eutectic mixture. *CrystEngComm* **2012**, *14*, 8365–8367. [CrossRef]
32. Stassen, I.; Styles, M.; Grenci, G.; Van Gorp, H.; Vanderlinden, W.; De Feyter, S.; Falcaro, P.; De Vos, D.; Vereecken, P.; Ameloot, R. Chemical vapour deposition of zeolitic imidazolate framework thin films. *Nat. Mater.* **2016**, *15*, 304–310. [CrossRef] [PubMed]
33. Pilz, J.; Perrotta, A.; Leising, G.; Coclite, A.M. ZnO Thin Films Grown by Plasma-Enhanced Atomic Layer Deposition: Material Properties Within and Outside the "Atomic Layer Deposition Window". *Phys. Status Solidi* **2019**, *217*, 1900256. [CrossRef]
34. Pilz, J.; Tazreiter, M.; Coclite, A.M. Universal software for the real-time control of sequential processing techniques. *J. Vac. Sci. Technol. A* **2019**, *37*, 063201. [CrossRef]
35. Neuhold, A.; Brandner, H.; Ausserlechner, S.J.; Lorbek, S.; Neuschitzer, M.; Zojer, E.; Teichert, C.; Resel, R. X-ray based tools for the investigation of buried interfaces in organic electronic devices. *Org. Electron.* **2013**, *14*, 479–487. [CrossRef] [PubMed]
36. Schrode, B.; Pachmajer, S.; Dohr, M.; Röthel, C.; Domke, J.; Fritz, T.; Resel, R.; Werzer, O. GIDVis: A comprehensive software tool for geometry-independent grazing-incidence X-ray diffraction data analysis and pole-figure calculations. *J. Appl. Crystallogr.* **2019**, *52*, 683–689. [CrossRef]
37. Rasband, W. ImageJ. Available online: https://imagej.nih.gov/ (accessed on 20 August 2021).
38. Necas, D.; Klapetek, P. Gwyddion. Available online: http://gwyddion.net/ (accessed on 20 August 2021).
39. Haynes, W.M. *CRC Handbook of Chemistry and Physics*, 92nd ed.; CRC Press: Boca Raton, FL, USA, 2011.

40. Cruz, A.J.; Arnauts, G.; Obst, M.; Kravchenko, D.E.; Vereecken, P.M.; De Feyter, S.; Stassen, I.; Hauffman, T.; Ameloot, R. Effect of different oxide and hybrid precursors on MOF-CVD of ZIF-8 films. *Dalton Trans.* **2021**, *50*, 6784–6788. [CrossRef]
41. Kwon, H.T.; Jeong, H.K.; Lee, A.S.; An, H.S.; Lee, T.; Jang, E.; Lee, J.S.; Choi, J. Defect-induced ripening of zeolitic-imidazolate framework ZIF-8 and its implication to vapor-phase membrane synthesis. *Chem. Commun.* **2016**, *52*, 11669–11672. [CrossRef]
42. Bons, A.J.; Bons, P.D. The development of oblique preferred orientations in zeolite films and membranes. *Microporous Mesoporous Mater.* **2003**, *62*, 9–16. [CrossRef]
43. Drift, A.; van der Selection, E. A Principle Governing Growth Orientation in Vapour-deposited Layers. *Philips Res. Repts* **1967**, *22*, 267–288.
44. Karagiaridi, O.; Lalonde, M.B.; Bury, W.; Sarjeant, A.A.; Farha, O.K.; Hupp, J.T. Opening ZIF-8: A catalytically active zeolitic imidazolate framework of sodalite topology with unsubstituted linkers. *J. Am. Chem. Soc.* **2012**, *134*, 18790–18796. [CrossRef] [PubMed]
45. CCDC: Mercury. Available online: https://www.ccdc.cam.ac.uk/Community/csd-community/freemercury/ (accessed on 15 March 2020).